CONDENSED MATTER PHYSICS

Anisotropic strain relaxation-induced directional ultrafast carrier dynamics in RuO_2 films

Seung Gyo Jeong[1]*†, In Hyeok Choi[2]*†, Seungjun Lee[3]*†, Jin Young Oh[4], Sreejith Nair[1], Jae Hyuck Lee[5], Changyoung Kim[5], Ambrose Seo[6], Woo Seok Choi[4], Tony Low[3]*, Jong Seok Lee[2]*, Bharat Jalan[1]*

Ultrafast light-matter interactions inspire potential functionalities in picosecond optoelectronic applications. However, achieving directional carrier dynamics in metals remains challenging due to strong carrier scattering within a multiband environment, typically expected for isotropic carrier relaxation. In this study, we demonstrate epitaxial RuO_2/TiO_2 (110) heterostructures grown by hybrid molecular beam epitaxy to engineer polarization selectivity of ultrafast light-matter interactions via anisotropic strain engineering. Combining spectroscopic ellipsometry, x-ray absorption spectroscopy, and optical pump-probe spectroscopy, we revealed the strong anisotropic transient optoelectronic response at an excitation energy of 1.58 eV in strain-engineered RuO_2/TiO_2 (110) heterostructures along both in-plane [001] and [1$\bar{1}$0] crystallographic directions. Theoretical analysis identifies strain-induced modifications in band nesting as the underlying mechanism for enhanced anisotropic carrier relaxation observed at this excitation energy. These findings establish epitaxial strain engineering as a powerful tool for tuning anisotropic optoelectronic responses with near-infrared excitations in metallic systems, paving the way for next-generation polarization-sensitive ultrafast optoelectronic devices.

INTRODUCTION

The study of light-matter interactions has garnered much attention in condensed matter physics and materials science, particularly for its role in enabling next-generation optoelectronic technologies. A key area of interest is the engineering of strong polarization selectivity in these interactions, which offers great potential for advancing optoelectronic applications, such as polarization-sensitive photodetectors (*1*–*4*), linearly polarized light emitters (*5*, *6*), and systems for optical communication (*7*), imaging (*8*), and high-speed digital signal transmission (*9*). Central to these applications is the anisotropy of transient photo response in the picosecond regime, which enables the realization of ultrafast optical switches and modulators. These ultrafast optoelectronic devices, controlled by light polarization, are critical for the next generation of optical information processing technologies (*10*, *11*).

Previous studies have largely focused on correlated metallic systems, where anisotropic behavior has been relatively small and restricted to cryogenic temperatures (*12*–*21*), especially for the transient optical response. Such limitations pose a challenge for practical applications, particularly in room-temperature environments. Recent advancements in the study of low-symmetry insulating two-dimensional (2D) materials have revealed transient optoelectronic anisotropy at room temperature (*10*, *22*–*29*). These present exciting opportunities for developing scalable, stable ultrafast optoelectronic devices capable of functioning under ambient conditions. However, conventional fabrication methods for 2D materials, including mechanical exfoliation (*30*, *31*), have encountered major challenges related to scalability and environmental stability, which hinder their practical implementation in large-scale applications. In addition, the anisotropy of materials is inherently determined by the crystal structure and severely limits the degree of tunable anisotropy for engineering specific optical functionalities.

Epitaxial rutile oxide heterostructures provide a promising platform for achieving optoelectronic anisotropy by harnessing anisotropic epitaxial strain. As illustrated in Fig. 1A, TMO_6 octahedra (TM: transition metal) in the (110) rutile structure is edge shared along the [001] direction, where the octahedra at the corner of the unit cell are connected via edge-sharing of equatorial oxygen atoms (gray arrow). In contrast, along the [1$\bar{1}$0] direction (purple arrow), the octahedra exhibit corner-sharing, involving both equatorial oxygen atoms from the primitive sublattice and apical oxygen atoms from the centered sublattice. This innate structural anisotropy in the rutile structure can lead to the anisotropic electronic band structures resulting in polarization-selective optoelectronic responses. By constructing epitaxial RuO_2/TiO_2 (110) heterostructures, additional structural anisotropy can be introduced through epitaxial strain (*32*–*34*). For instance, the lattice mismatch between RuO_2 film grown on TiO_2 (110) bulk is −4.7% along [001], creating compressive strain, and +2.3% along [1$\bar{1}$0], generating tensile strain. Furthermore, the large compressive [001] strain can induce the anisotropic strain relaxation starting at 4 nm RuO_2 film thickness, while the tensile [1$\bar{1}$0] strain is well preserved until 17 nm, leading to anisotropic strain relaxations (*32*). These anisotropic epitaxial strain effects provide a scalable platform for engineering anisotropic light-matter interactions in this metallic system, opening exciting possibilities for polarization-sensitive ultrafast optoelectronics.

In this paper, we demonstrated both static and dynamic electronic anisotropy engineering in strain-controlled RuO_2 films via epitaxial design. Using hybrid molecular beam epitaxy (hMBE), we

[1]Department of Chemical Engineering and Materials Science, University of Minnesota–Twin Cities, Minneapolis, MN 55455, USA. [2]Department of Physics and Photon Science, Gwangju Institute of Science and Technology (GIST), Gwangju 61005, Republic of Korea. [3]Department of Electrical and Computer Engineering, University of Minnesota, Minneapolis, MN 55455, USA. [4]Department of Physics, Sungkyunkwan University, Suwon 16419, Republic of Korea. [5]Department of Physics and Astronomy, Seoul National University, Seoul 08826, Republic of Korea. [6]Department of Physics and Astronomy, University of Kentucky, Lexington, KY 40506, USA.
*Corresponding author. Email: jeong397@umn.edu (S.G.J.); jys2316@gm.gist.ac.kr (I.H.C.); seunglee@umn.edu (S.L.); tlow@umn.edu (T.L.); jsl@gist.ac.kr (J.S.L.); bjalan@umn.edu (B.J.)
†These authors contributed equally to this work.

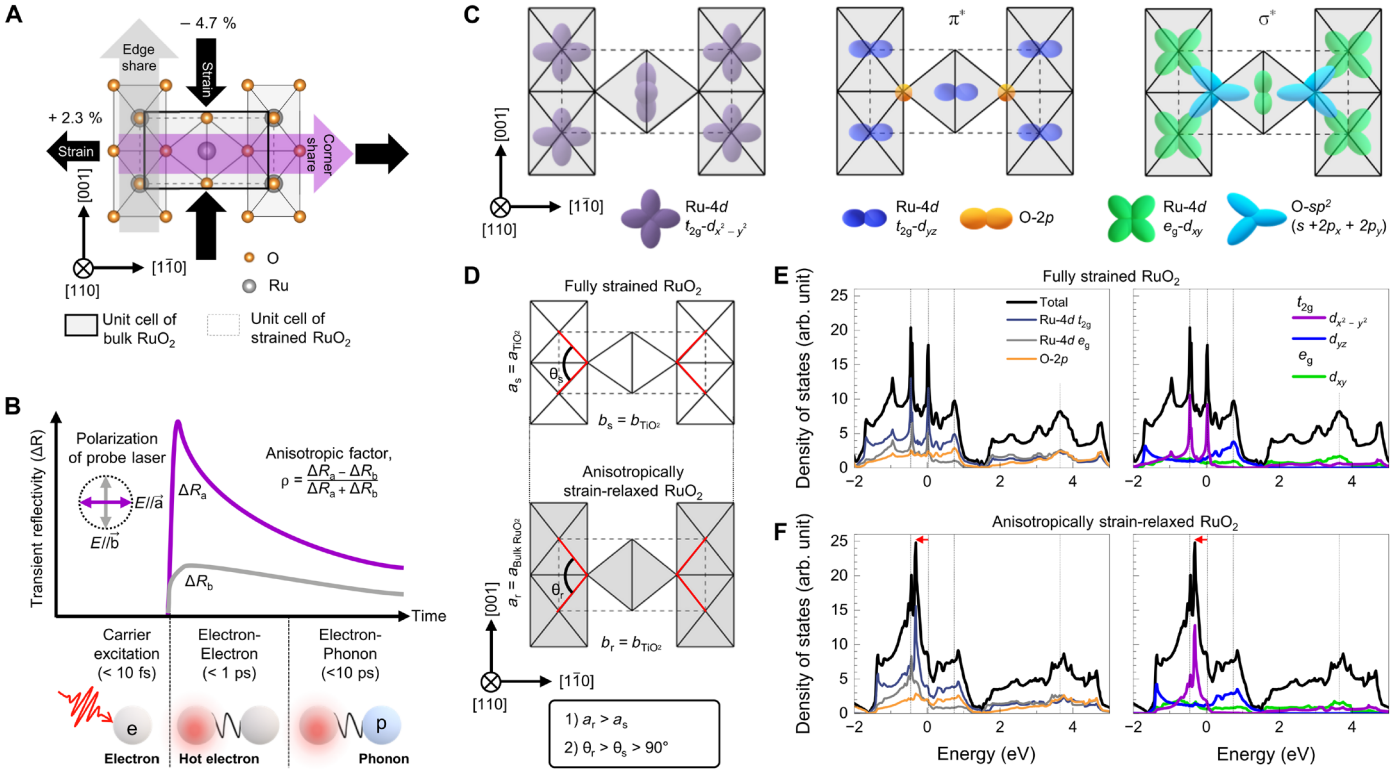

Fig. 1. Epitaxial strain control of electronic anisotropy in the RuO_2/TiO_2 (110) heterostructure. (**A**) Schematic illustrates anisotropic ionic bonding in the RuO_2 (110) heterostructure with anisotropic epitaxial strain (black arrows) on TiO_2 (110) substrate. The strain values are estimated based on bulk lattice parameters. (**B**) Schematic illustration of ΔR as a function of time delay using an optical pump probe demonstrates an experimental example of transient electronic anisotropy. The bottom panels show the dominant carrier dynamics excited by pumping laser with different ultrafast timescales. (**C**) Schematic representations of three representative orbital states projected on the RuO_2 (110) plane. (**D**) Schematics of the RuO_2 model systems are adopted for DFT calculations to describe anisotropic strain relaxations along the [001] direction. The anisotropic strain relaxation yields two structural evolutions: (i) $a_r > a_s$ and (ii) $\theta_r > \theta_s > 90°$, as discussed in the main text. (**E** and **F**) The density of states projected by Ru-4*d* and O-2*p* states (left panels) and detailed Ru-4*d* states ($d_{x^2-y^2}$, d_{yz}, and d_{xy}, right panels) for (E) fully strained and (F) anisotropically strain-relaxed RuO_2. The vertical dotted lines are each peak position of the orbital states for the fully strained case. The red arrows indicate the [001] strain relaxation–induced energy shift of the $d_{x^2-y^2}$ state.

synthesized atomically flat RuO_2 films (*32*, *35*) of varying thicknesses on TiO_2 (110) (figs. S1 to S3). Combining x-ray absorption spectroscopy (XAS), spectroscopic ellipsometry, and density functional theory (DFT) calculations, we identified that anisotropic strain relaxation effectively modulates the static optical anisotropy in RuO_2, starting at ~4 nm film thickness, consistent with an optical second harmonic generation (SHG) study (*32*). Furthermore, optical pump-probe spectroscopy reveals obvious anisotropy in hot carrier dynamics, demonstrating its tunability via anisotropic strain relaxation. Theoretical analysis on electronic band structures highlighted strain-tunable band nesting in the Ru-4*d* t_{2g} states of RuO_2, as the key mechanism driving directionally selective hot carrier dynamics for anisotropically strain-relaxed RuO_2. These findings establish substantial room-temperature optical anisotropy in metallic oxides, offering an exciting strategy to design polarization-sensitive ultrafast optoelectronic devices using epitaxially strained rutile heterostructures.

RESULTS

To quantify the polarization-selective dynamic optical anisotropy, we probe the transient reflectivity change (ΔR) in response to ultrashort laser pulses using a femtosecond laser. By measuring ΔR along different crystallographic axes (see Fig. 1B), such as the *a* and *b* axes, the dynamic optical anisotropy between these orientations can be quantified by the parameter $\rho = (\Delta R_a - \Delta R_b)/(\Delta R_a + \Delta R_b)$, as similarly defined in previous studies (*27*, *36*). This approach further enables the disentangling of the time-dependent contributions of various carrier dynamics (*10*, *37*). Within the first picosecond (<1 ps), carrier scattering dominated by electron-electron scatterings plays a key role, while electron-phonon coupling becomes more prominent in the sub–10-ps regime as carriers thermalize with the lattice (*38*), as schematically shown in the bottom panels of Fig. 1B. These indicate that static electronic and structural anisotropies, as well as their carrier dynamics, are essential for transient optical anisotropy in materials.

We first discuss the crystal structure of RuO_2/TiO_2 (1$\bar{1}$0) and the orbital hybridization along two in-plane directions [1$\bar{1}$0] and [001]. Figure 1C shows three key orbital states in the (110) plane of rutile RuO_2 that influence its electronic structure near the Fermi level (*39*–*41*). The Ru-4*d* orbitals split into three t_{2g} states ($d_{x^2-y^2}$, d_{xz}, and d_{yz}) and two e_g states (d_{xy} and d_{z^2}). The $d_{x^2-y^2}$ orbitals, directed toward neighboring Ru atoms, are nonbonding with O-2*p* orbitals (left panel of Fig. 1C), whereas the d_{yz} orbitals form π* antibonding

with O-2p_z (middle panel of Fig. 1C) and O-2p_y of the apical oxygen in the primitive octahedra (*40*). The coordinate axes are defined as x = [001], y = [1$\bar{1}$0], and z = [110], following previous literature (*33*, *34*). The d_{xy} orbital forms σ* antibonding with the sp^2 type of O orbitals owing to the trigonal-like coordination of Ru and O atoms along the corner sharing direction (right panel of Fig. 1C). Given these bonding configurations, it is reasonable to expect that anisotropic strain relaxation, which modifies both bond angles and bond lengths, can effectively alter the electronic structure of RuO_2/TiO_2 (110), leading to tunable anisotropic optical and transport responses.

To investigate this, we performed DFT calculations. Specifically, we modeled two cases as depicted schematically in Fig. 1D: (i) fully strained RuO_2 with lattice constants in both [001] and [1$\bar{1}$0] directions matching the TiO_2 (110) substrate [$a_s = a_{TiO2.}$ and $b_s = b_{TiO2}$, where a_s and b_s refer to the lattice parameters of a fully strained RuO_2 film, and a_{TiO2} and b_{TiO2} denote lattice parameters of the TiO_2 (110) substrate along two in-plane directions], and (ii) anisotropically strain-relaxed RuO_2 (110) with the [001] lattice constant matching bulk RuO_2 while [1$\bar{1}$0] remains fully strained by TiO_2 ($a_r = a_{bulk\ RuO2}$ and $b_r = b_{TiO2}$, where a_r and $a_{bulk\ RuO2}$ refer to the relaxed lattice parameter and bulk lattice parameter of RuO_2 along [001] direction and b_r is the lattice parameter of RuO_2 along [1$\bar{1}$0]). Figure 1D illustrates the corner bonding geometry along [1$\bar{1}$0], showing that $a_r > a_s$ and $\theta_r > \theta_s > 90°$, where θ_s and θ_r represent the Ru-O-Ru bonding angles in fully strained and anisotropically strain-relaxed RuO_2, respectively. This structural change strongly influences orbital hybridization and electronic properties. We note that the two strain conditions as illustrated in Fig. 1D were chosen to evaluate the effect of anisotropic strain relaxation in RuO_2/TiO_2 (110) on the electronic structure.

Figure 1 (E and F) shows the orbital projected density of states for fully strained and anisotropically strain-relaxed RuO_2, as depicted in Fig. 1D, respectively. The solid black lines in the left and right panels represent the total density of states near the Fermi level. While the left panels display projected Ru-4*d* t_{2g}, e_g, and O-2*p* orbitals, the right panels show detailed orbital projections of Ru-4*d* t_{2g} and e_g. The Fermi level of RuO_2 is located within the Ru-t_{2g} states, which governs its metallic behavior. More specifically, the projected Ru-4*d* states in the right panels reveal that the two peaks near the Fermi level are primarily associated with the $d_{x^2-y^2}$ orbital states, and subsequent peaks above the Fermi level are mainly related to π^* of d_{yz} and σ^* of d_{xy}. The t_{2g} states ($d_{x^2-y^2}$ and d_{yz}) exhibit a peak-like structure, where the density of states concentrates within a narrow energy range, indicating the weak orbital overlap characteristic of lateral π bonding (*39*, *40*). In contrast, the e_g state (d_{xy}) shows a much broader bandwidth in which the density of states extends across a wide energy range, attributed to the larger head-on overlap of σ-type bonding (*39*, *40*). Furthermore, the density of states of the O-2*p* state exhibits similar behavior to that of the Ru states, indicating strong Ru-O hybridization of RuO_2. When the strain along [001] is anisotropically relaxed to bulk RuO_2 (while the strain along [1$\bar{1}$0] is preserved), the bandwidth of all π^* and σ^* bonding states becomes larger and the peak position of π^* bonding of d_{yz} states shifts to a higher energy. The former suggests the larger Ru-O orbital overlap in strain-relaxed cases. This further indicates that larger θ_r by strain relaxation along the [001] direction, as shown in Fig. 1E, is crucial in determining the Ru-O hybridization rather than the increase in a_r. On the other hand, the anisotropic strain relaxation along [001] also induces the energy lowering of the $d_{x^2-y^2}$ state (indicated by the red arrows in Fig. 1F), consistent with the previous studies (*33*, *34*, *40*).

To examine the anisotropy of Ru-O orbital hybridization in epitaxial RuO_2/TiO_2 (110) heterostructures, we performed XAS as shown in Fig. 2, with total electron-yield (TEY) mode (*42*), at the O *K*-edge because it is strongly coupled with Ru-O hybridized orbitals. The TEY mode is a surface-sensitive technique with a probing depth of only a few nanometers (*42*). Figure 2A shows the schematic of the setup illustrating how O *K*-edge XAS spectra are acquired with $E_{[1\bar{1}0]}$ (electrical field is along [1$\bar{1}$0] direction) and $E_{[001]}$ (electrical field is along [001]) direction polarized light with an incidence angle of 90°. Before discussing the experimental data, we examine the DFT calculations presented in Fig. 2B. These calculations project the density of states for unoccupied O-2*p* orbitals along two distinct in-plane crystal orientations: 2p_x along [001] and 2p_y along [1$\bar{1}$0]. This projection simulates the XAS-related band structures. Because O-2p_z orbitals do not contribute to the O *K*-edge XAS spectrum in the (110) surface normal incidence configuration, our focus is on the 2p_x and 2p_y orbital states. The first peak near 1 eV (in Fig. 2B) is predominantly associated with 2p_y orbital (π^*-type bonding with t_{2g} states), while the broader peak around 3.7 eV involves a combination of 2p_x and 2p_y orbitals (σ^*-type bonding with e_g states). Considering the strain effect along the [001] direction between fully strained (top panel) and anisotropically strain-relaxed RuO_2 (bottom panel), for both π^* and σ^* peaks, the bandwidths become broader with strain relaxation, while the peak positions of strain-relaxed RuO_2 shift to higher energy compared to that of fully strained RuO_2 (vertical dotted lines), indicating increase of the Ru-O hybridization due to anisotropic strain relaxations, consistent with the conduction band of Ru-4*d* states in Fig. 1 (E and F).

We now turn to the discussion of experimental results. Figure 2C shows XAS spectra with $E_{[001]}$ (upper black) and $E_{[1\bar{1}0]}$ polarization (lower purple) for 2-, 4-, and 12-nm RuO_2 films. Each spectrum was normalized by the peak intensity at 532 eV. The vertical dotted lines for the 2-nm RuO_2 film (left panel) show the two peak positions at ~529 and ~532 eV of t_{2g}-π^* and e_g-σ^* states, respectively, in agreement with the previous rutile studies (*40*, *43*, *44*). Especially for $E_{[1\bar{1}0]}$ polarization, [1$\bar{1}$0] directional electric field shows a much stronger t_{2g}-π^* peak, consistent with the dominant contribution of 2p_y orbital for the t_{2g}-π^* state shown in Fig. 2B. As RuO_2 thickness (d) increases, both relative peak intensity [$I(t_{2g})/I(e_g)$] and separation (Δ) between t_{2g}-π^* and e_g-σ^* peaks increase (plotted in Fig. 2, D and E). Furthermore, the thickness dependence of $I(t_{2g})/I(e_g)$ in $E_{[001]}$ polarization XAS is relatively smaller compared to $E_{[1\bar{1}0]}$, leading to the thickness modulations of electronic structure anisotropy in RuO_2 (110) films.

The $I(t_{2g})/I(e_g)$ at O *K*-edge XAS is proportional to the Ru-O orbital hybridization strength and the number of unoccupied Ru states (*45*). Because the Ru *L*-edge XAS spectrum in fig. S4 shows the robust +4 oxidation state for our RuO_2 (110) films, the increase in $I(t_{2g})/I(e_g)$ with film thickness indicates enhancement of Ru-O hybridization with strain relaxations. In addition, x-ray photoemission spectroscopy (fig. S5) confirm the +4 oxidation states of Ru in these films. We note that the enhancements of $I(t_{2g})/I(e_g)$ in XAS are more pronounced compared to our DFT calculations, which might suggest the additional strain effect such as structural phase transition (*32*) and/or dimensional crossover. This may also be attributed to the multiplet effects in XAS, arising from interactions between

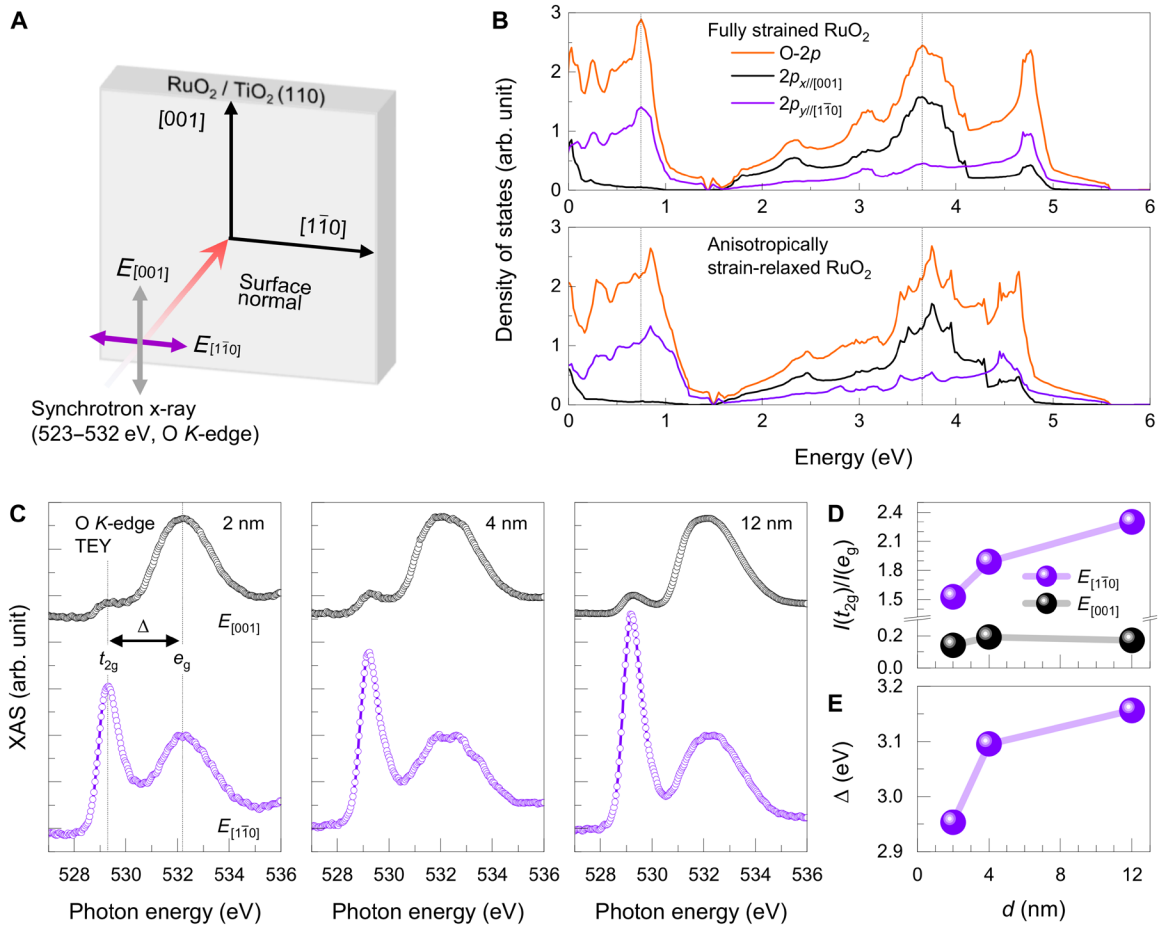

Fig. 2. Modulated anisotropic Ru-O hybridizations of epitaxial RuO_2/TiO_2 (110) heterostructures. (**A**) Schematic of the scattering geometry with the surface normal incident synchrotron x-ray beam. $E_{[001]}$ and $E_{[1\bar{1}0]}$ polarizations are parallel to the [001] and [1$\bar{1}$0] directions of RuO_2/TiO_2 (110) samples, respectively. (**B**) The density of states for O-2*p* orbitals are projected to the [001] ($2p_x$) and [1$\bar{1}$0] ($2p_y$) direction for fully strained (bottom) and anisotropically strain-relaxed RuO_2 films (top). (**C**) XAS spectra at the O *K*-edge measured by TEY methods show $E_{[1\bar{1}0]}$ (purple) and $E_{[001]}$ (black) polarization dependence for RuO_2 thicknesses of 2, 4, and 12 nm in RuO_2/TiO_2 (110). Vertical dotted lines represent the peak positions indicating Ru-4*d* t_{2g} and e_g with O-2*p* hybridizations with their energy difference, Δ, for the 2-nm case. (**D**) $I(t_{2g})/I(e_g)$ and (**E**) Δ show RuO_2 thickness dependence due to the anisotropic strain relaxations. The $I(t_{2g})/I(e_g)$ was assigned based on the point of highest intensity for each t_{2g}-and e_g-related peak.

core-hole states and valence electrons (*46*), which are not accounted for in our DFT calculations. On the other hand, because the anisotropic strain relaxation effect is more pronounced in the strongly bonded e_g-σ^* states compared to the t_{2g}-π^* bonding states (*40*), this leads to a clear peak shift for the e_g-σ^* state, resulting in the enhanced Δ. Thus, we attribute the increase of Δ and $I(t_{2g})/I(e_g)$ above 4 nm RuO_2 films originating from the strain relaxation–induced evolution in the electronic structure. We could not observe a specific thickness-dependent bandwidth change for each XAS peak, which might be due to the peak broadness caused by photoelectron damping. Nevertheless, the combined experimental XAS data and DFT calculations show how thickness and anisotropic strain relaxation along [001] results in the anisotropic electronic structure of RuO_2 films.

Last, we investigate in Fig. 3 the polarization-selective optical anisotropy and carrier dynamics in RuO_2 (110) films by measuring the transient reflectivity change ΔR in response to ultrashort laser pulses using a femtosecond laser. Figure 3A shows the ΔR in the picosecond time domain for epitaxial RuO_2 (110) films of varying thicknesses. Both pump and probing laser have a center wavelength of 785 nm (1.58 eV) as illustrated in Fig. 3C to selectively excite and monitor the anisotropic Ru t_{2g}-related transitions. The polarization of the pump laser was applied along the [001] direction whereas the transient optical reflectivity as a function of time, the ΔR, was measured with two different polarization angles (θ) of probing laser pulse (θ = 0° for $E_{[1\bar{1}0]}$ and θ = 90° for $E_{[001]}$) for RuO_2 films of thicknesses 4, 7, and 12 nm. Data from other film thicknesses (2 and 17 nm) are shown in fig. S6. Because the optical penetration depth of RuO_2 is estimated to be ~26 nm from ellipsometry results, we confirmed that the entire film thickness was probed. The ΔR at this timescale depends only on the polarization of the probing laser but remains independent of the polarization of the pump laser (fig. S7). This indicates that the observed anisotropic hot carrier dynamics are intrinsic to the material's light-matter interaction, rather than dictated by the initial excitation conditions. Therefore, we focus on the polarization dependence of the probing laser. Figure 3A reveals that the difference in ΔR between

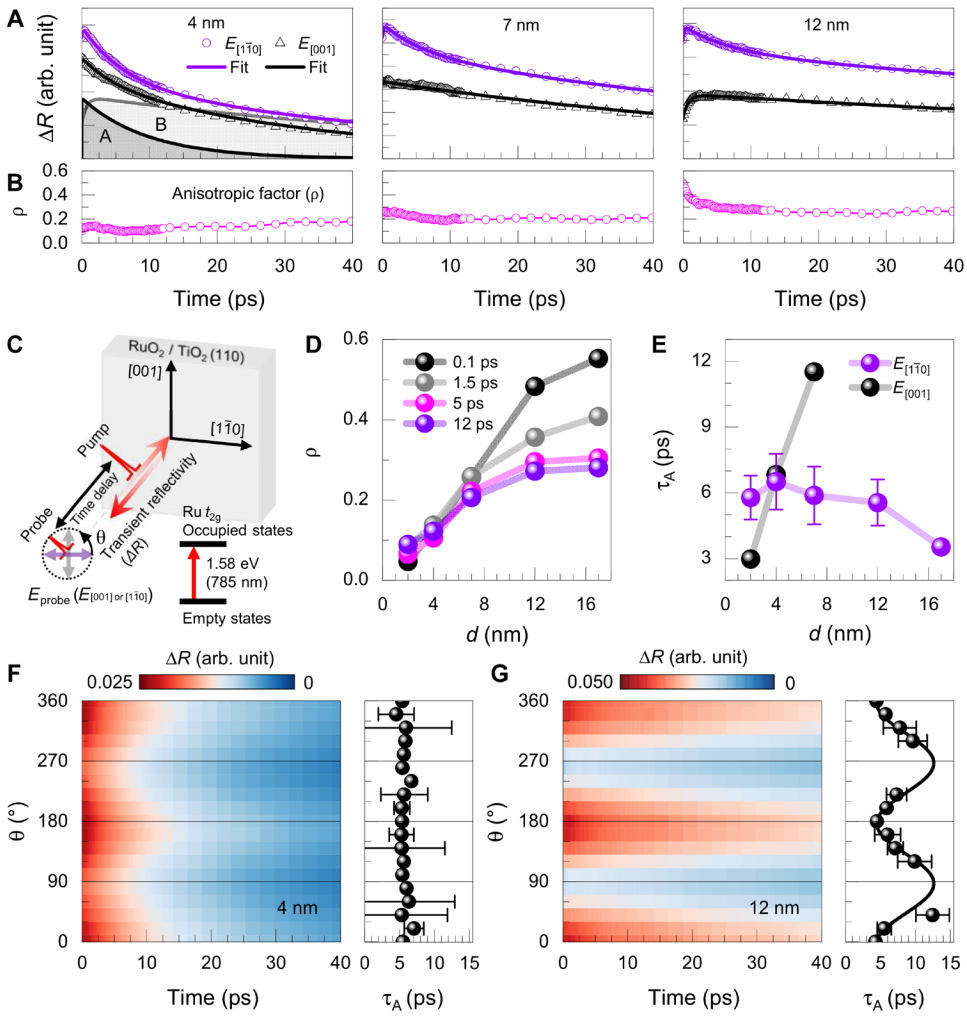

Fig. 3. Anisotropic ultrafast carrier dynamics of epitaxial RuO_2/TiO_2 (110) heterostructures. (**A**) Transient reflectivity change (ΔR) of RuO_2/TiO_2 (110) films for two perpendicular polarizations of the probe laser along [1$\bar{1}$0] and [001] of the crystal axis with (**B**) anisotropic factor, ρ. (**C**) Schematic of the scattering geometry with surface normal incident optical pump-probe measurement. (**D**) Time-dependent ρ and (**E**) polarization-dependent anisotropic τ_A with different film thicknesses (*d*). Polarization angle (θ) resolved ΔR (left) with τ_A (right) for (**F**) 4-nm and (**G**) 12-nm RuO_2 cases. The solid line of $\tau_A(\theta)$ is shown as a guide to the eye for the sine function.

the two probe polarizations ($E_{[1\bar{1}0]}$ and $E_{[001]}$) becomes increasingly pronounced as anisotropic strain relaxation increasing thickness *d*. More specially, as *d* increases, the decay slope of ΔR for $E_{[001]}$, where the electrical field is along the anisotropic strain relaxation direction, decreases. In contrast, the ΔR of the bulk RuO_2 (110) single crystal exhibits a negligible anisotropic behavior along both in-plane [1$\bar{1}$0] and [001] directions (fig. S8), which is consistent with static optical spectra of bulk RuO_2 (*47*, *48*). Figure 3B shows the anisotropic factor ρ as a function of time. As *d* increases, ρ increases for all time (*t*). Notably, the value of ρ for $t \leq 5$ ps is larger than that for $t > 5$ ps, indicating variations in dominant carrier dynamics depending on the timescale. To examine this further, we plot in Fig. 3D the optical anisotropy ρ as a function of *d* for selected *t* of 0.1, 1.5, 5, and 12 ps. Regardless of different timescales, the value of ρ remains nearly unchanged for $d \leq 4$ nm, whereas it becomes much larger for a smaller timescale (≤1.5 ps) for $d > 4$ nm. The highest ρ value of anisotropically strain-relaxed films ($d > 4$ nm) below 1 ps suggests an important role of electron-electron scatterings in the nonequilibrium state in determining transient optical anisotropy. At 0.1 ps, electron-electron scattering dominates the hot carrier dynamics, and then electron-phonon scattering becomes crucial until 12 ps. In Fig. 3A of the anisotropically strain-relaxed 12-nm film, ΔR of $E_{[001]}$ exhibits a more gradual rise in ΔR below 2 ps compared to that of $E_{[1\bar{1}0]}$, resulting in a large difference of ρ values. The slower electron-electron thermalization time for $E_{[001]}$ (but not for $E_{[1\bar{1}0]}$) indicates an anisotropic reduction of electron-electron scattering along the [001] direction.

We further fit the anisotropic ΔR using two exponential components, A and B, shown in Fig. 3A. Because the fast decay component A in $E_{[001]}$ above 12 nm disappears (fig. S6), we only included the slow decay component B in those cases. Figure 3E shows thickness-dependent decay time for the A component (τ_A). In strained films below 4 nm, the τ_A value of $E_{[001]}$ is much smaller than that of $E_{[1\bar{1}0]}$, and it increases and disappears above 12 nm as thickness increases. On the other hand, the τ_A value of $E_{[1\bar{1}0]}$ starts to decrease above 4 nm, and it lastly becomes much faster than that of $E_{[001]}$.

This opposing tendency between $E_{[001]}$ and $E_{[1\bar{1}0]}$ induces and increases the anisotropy in the carrier dynamics with increasing film thickness. The evolutions of anisotropy with thickness are also confirmed in electrical transports using the two Hall bar devices along the [001] and [1$\bar{1}$0] directions of RuO_2 (110) films, as shown in fig. S9 (*49*). Figure 3 (F and G) shows more detailed θ-resolved ΔR contour plots with fitting results of τ_A for the 4- and 12-nm RuO_2 film, respectively. Both $\Delta R(\theta)$ contour plot and $\tau_A(\theta)$ of 12 nm show strong twofold anisotropy, whereas those of 4 nm exhibit weak anisotropy. Figure S10 further exhibits the same twofold anisotropy for the 17-nm case. More specifically for the 12-nm film, when θ is close to 90° or 270° parallel to the anisotropically strain-relaxed [001] crystal axis, τ_A becomes larger and merges to the slow B component at 90° or 270°. In contrast to the appearance of transient anisotropy at cryogenic temperature for Sr_2RuO_4 (*12*), the anisotropy between $E_{[001]}$ and $E_{[1\bar{1}0]}$ of 4- and 12-nm RuO_2 films increases with anisotropic enhancement of ΔR for $E_{[1\bar{1}0]}$ as temperature increases (figs. S11 and S12), with the optical anisotropy persisting over a wide range of temperatures.

The anisotropic transient behavior in ΔR can originate from two possible mechanisms: instantaneous anisotropic carrier distribution or anisotropic carrier transitions. The former arises from an uneven distribution of excited carriers across momentum states (*23*, *25*, *27*, *50*), while the latter is governed by direction-dependent optical transitions by the nonequilibrium population influenced by band structure asymmetry (*26*, *27*). Both effects have been observed in pump-probe measurements of anisotropic materials (*23*, *25*–*27*, *50*). However, the insensitivity of ΔR to the pump laser polarization effectively rules out the contribution of an anisotropic carrier distribution, indicating that the transient carriers have already reached a quasi-equilibrium state with an elevated electronic temperature upon the probe measurement. The decay of the ρ in the 12-nm film occurs within ~3 ps (Fig. 3A), which is consistent with the energy relaxation of thermally distributed carriers, rather than from anisotropic carrier populations across the Brillouin zone. Furthermore, the laser pulse width in our setup is approximately 160 fs, as measured by interference autocorrelation. Because this pulse duration exceeds the typical timescale for carrier-carrier momentum relaxation, the photoexcited anisotropic carrier distribution would not have survived for detection, further explaining the lack of pump polarization dependence. These suggest that the observed anisotropy in ΔR stems from transient anisotropic optical transitions of the probe beam along the [1$\bar{1}$0] and [001] directions; an effect solely due to the anisotropic electronic structure.

To investigate the origin of optical transient anisotropy, we first examine the anisotropic optical spectra of RuO_2 films using spectroscopic ellipsometry. Figure 4 (A and B) shows optical spectra of strain-relaxed 17-nm RuO_2 thin films (see texts S1 and S2 and figs. S13 and S14 for further details). Here, $\sigma_{1,o}(\omega)$ and $\sigma_{1,e}(\omega)$ are real parts of ordinary (along the [1$\bar{1}$0] direction) and extraordinary (along the [001] direction) optical conductivity spectra, respectively. Using Drude-Lorentz analysis, we extracted the individual spectra weight for four optical transitions (Lorentzian oscillators assigned by α, β, A, and γ) and free charge carrier contribution (Drude model). At the transition energy of 1.58 eV (i.e., at 785 nm of the pump/probe laser wavelength), both the Drude contribution and the Ru-4*d* $t_{2g} \rightarrow t_{2g}$ interband transitions (α and β transitions) contribute to the optical response. Figure 4 (C and D) exhibits distinct thickness dependence of $\sigma_{1,o}(\omega)$ and $\sigma_{1,e}(\omega)$ due to anisotropic strain relaxations, respectively. As thickness increases, spectra weight of $\sigma_{1,e}(\omega)$ above 1.5 eV increases compared to that of $\sigma_{1,o}(\omega)$, indicating the optical anisotropy in optical transitions for anisotropically strain-relaxed RuO_2. These results highlight the interplay between free carrier dynamics and interband transitions in governing the observed anisotropic optical response in strain-relaxed RuO_2.

We further explore the strain-dependent transient anisotropy of transition matrix elements by calculating the $\sigma_{1,o}(\omega)$ and $\sigma_{1,e}(\omega)$ with varying chemical potentials (δ) to simulate photoexcited carrier dynamics. In our DFT calculations, the transient increase in carrier density induced by photoexcitation within the few-picosecond regime is modeled by shifting the chemical potential as $\mu = \mu_0 + \delta$, where μ and μ_0 correspond to the chemical potentials of the excited and ground states, respectively. The corresponding theoretical evaluations of $\sigma_{1,o}(\omega)$ and $\sigma_{1,e}(\omega)$ are presented in Fig. 4 (E to H), showing the calculated interband contributions to $\sigma_{1,o}(\omega)$ and $\sigma_{1,e}(\omega)$ for anisotropically strain-relaxed (Fig. 4, E and F) and fully strained RuO_2 (Fig. 4, G and H). The transient state is captured by varying δ from 0 to 0.3 eV. In the ground state ($\delta = 0$), two prominent peaks appear near 0.7 and 1.2 eV, originating from Ru-4*d* $t_{2g} \rightarrow t_{2g}$ transitions, which is consistent with the experimental observation of α peak at ~0.7 eV. Our calculations also captured the effect of anisotropic strain relaxation: the peak intensities of the $t_{2g} \rightarrow t_{2g}$ transitions for $\sigma_{1,e}(\omega)$ are much stronger compared to those for $\sigma_{1,o}(\omega)$ in anisotropically strain-relaxed RuO_2 (Fig. 4, E and F), which is in agreement with the experimental results (peak intensity corresponding to α). In the excited state ($\delta > 0$), as δ increases, $\sigma_{1,e}(\omega)$ of anisotropically strain-relaxed RuO_2 shows relatively small variations, particularly above 1.3 eV (Fig. 4F), while that of fully strained RuO_2 exhibits noticeable changes in the same energy window (Fig. 4H). The $\sigma_{1,o}(\omega)$ of both strain-relaxed and strained RuO_2 increases with δ (Fig. 4, E and G). We note that the lack of dependence of $\sigma_{1,e}(\omega)$ for strain-relaxed RuO_2 and the slow decay of hot carriers along [001] for the 12-nm film (Fig. 3A) align with the transient ΔR observed in Fig. 3.

To understand this observation, we further examine the electronic band structures of fully strained and anisotropically strain-relaxed RuO_2, as shown in Fig. 5, depicting the band structure in the $k_x - k_y$ plane at $k_z = 0$ for intuitive visualization. For strain-relaxed RuO_2 in Fig. 5A, we observed two sets of nested bands along the Γ − X line (the zone center to the [001] direction), with energy differences ($E_C - E_V$) between the nested bands estimated to be 0.7 eV (V_1 and C_1, green lines) and 1.2 eV (V_2 and C_2, blue lines), corresponding to peak positions of Ru-4*d* $t_{2g} \rightarrow t_{2g}$ transitions in Fig. 4 (F and H). The existence of the nested bands along the [001] direction suggests van Hove singularities in their joint density of states. It also explains why optical transitions are immune to changes in δ, consistent with the δ independence of $\sigma_{1,e}(\omega)$. To further investigate the degree of band nesting, we visualize the C_2 and V_2 band structures away from the high symmetry lines (Fig. 5, C and D). The contour plots in the bottom plane of Fig. 5 (C and D) show the energy difference between the C_2 and V_2 bands ($E_{C2} - E_{V2}$) projected in the two-dimensional *k* space. For anisotropically strain-relaxed RuO_2 (Fig. 5C), robust band nesting, i.e., identical $E_{C2} - E_{V2}$ values, also occurs besides the Γ − X line, indicating nearly δ-independent $\sigma_{1,e}(\omega)$. On the other hand, for fully strained RuO_2 (Fig. 5, B and D), strain-induced lifting of degeneracy results in the splitting into C_2 and C'_2, reducing the degree of band nesting (decreasing $E_{C2} - E_{V2}$ values near X). This effect leads to a relatively pronounced δ dependence of $\sigma_{1,e}(\omega)$ (Fig. 5D). We also note that the anisotropic δ

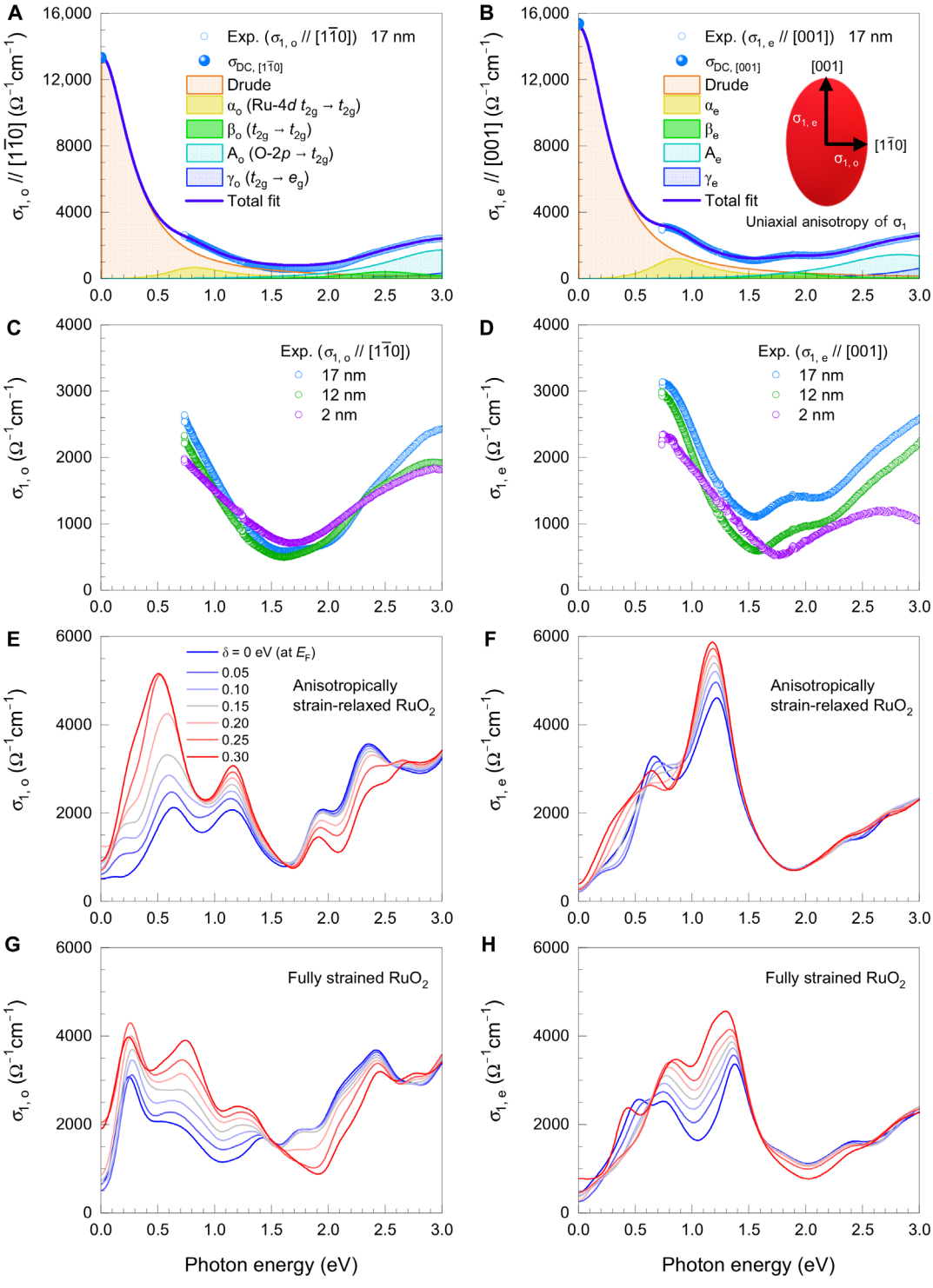

Fig. 4. Anisotropic optical conductivity spectra from experiment and DFT calculations. (**A**) $\sigma_{1,o}(\omega)$ along the [1$\bar{1}$0] direction and (**B**) $\sigma_{1,e}(\omega)$ along the [001] direction of the anisotropically strain-relaxed 17-nm RuO_2 (110) film. The shaded area indicates the estimated optical transitions including a single Drude model and Lorentzian oscillators. Schematic in (B) shows the uniaxial anisotropic model adopted in optical spectrum analysis. (**C**) $\sigma_{1,o}(\omega)$ and (**D**) $\sigma_{1,e}(\omega)$ show anisotropic thickness dependence related to the anisotropic strain relaxation along the [001] direction in RuO_2/TiO_2 (110). Interband contributions of $\sigma_{1,e}(\omega)$ and $\sigma_{1,o}(\omega)$ for (**E** and **F**) anisotropically strain-relaxed RuO_2 and (**G** and **H**) fully strained RuO_2 calculated by DFT with a modified chemical potential ($\mu = \mu_0 + \delta$).

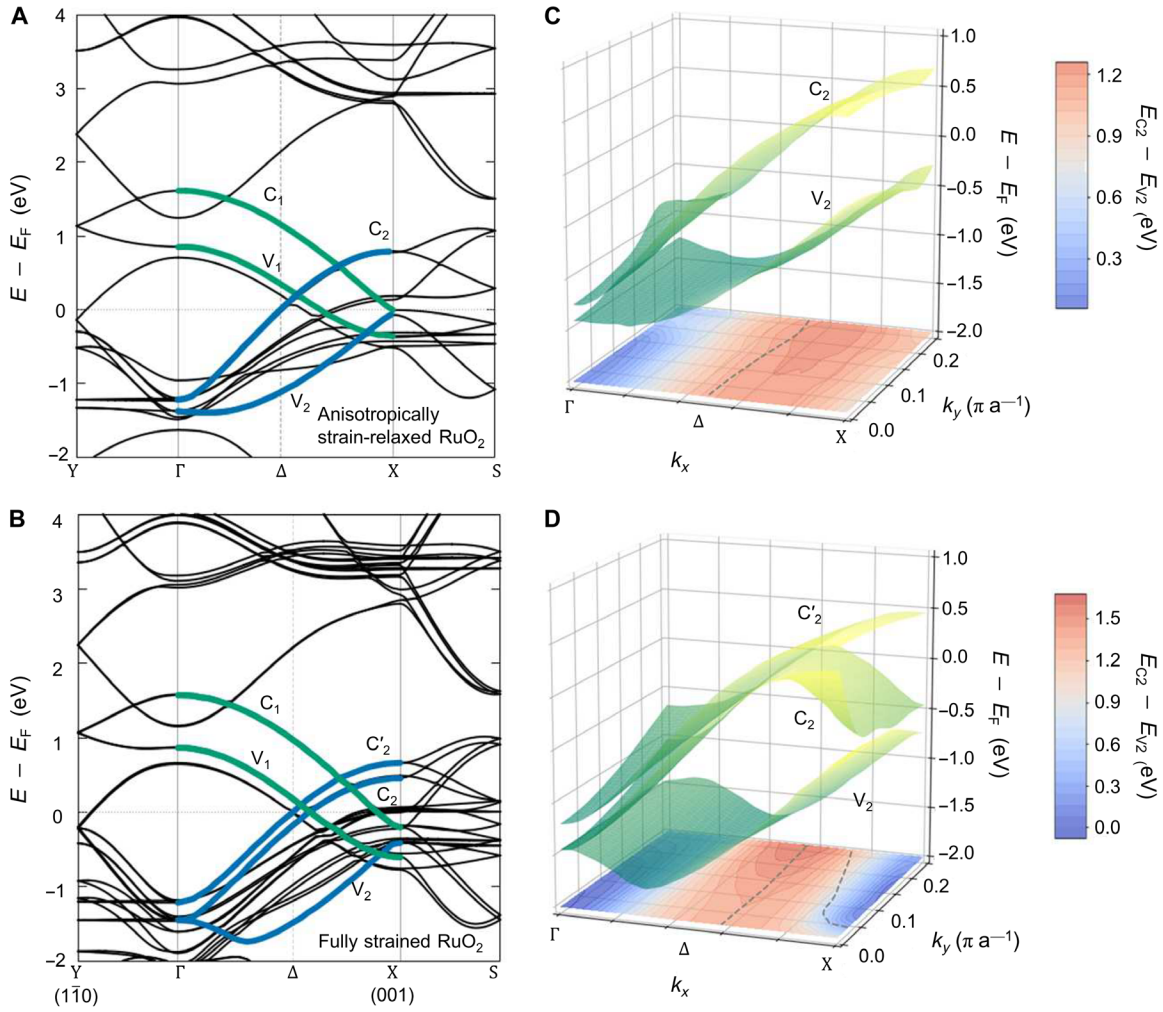

Fig. 5. Strain-controlled electronic band nesting. Electronic structures along the in-plane high-symmetry line and the nested bands on the two-dimensional *k* mesh for (**A** and **C**) anisotropically strain-relaxed RuO_2 and (**B** and **D**) fully strained RuO_2. The color contour maps in the bottom plane show the $E_{C2} - E_{V2}$ values and the gray dashed line indicates the zero-energy level of the C_2 band, indicating *k* space allowing optical transition ($C_2 > 0$ and $V_2 < 0$).

independence of $\sigma_{1,e}(\omega)$ aligns with the temperature-independent ΔR and τ_A for $E_{[001]}$ exclusively in the anisotropically strain-relaxed RuO_2 (fig. S11D). Theoretical analysis reveals that strain-induced modifications in band nesting underlie the enhanced anisotropic carrier relaxation experimentally observed at the excitation energy of 1.58 eV (Fig. 4), highlighting how anisotropic strain relaxation effectively tunes band nesting. These results demonstrate that strain relaxation offers a viable pathway to control transient optical responses in metallic epitaxial RuO_2 films.

DISCUSSION

In summary, we realized an unexpected yet systematic modulation of electronic anisotropy in metallic RuO_2 heterostructures by epitaxial strain control. DFT calculations revealed the anisotropic strain-dependent electronic structure with an enhancement of orbital hybridizations due to the anisotropic strain relaxation along the [001] direction. Following the theoretical insights of DFT, comprehensive observations of XAS, spectroscopic ellipsometry, and optical pump-probe techniques for RuO_2/TiO_2 (110) films confirmed the large enhancement of anisotropy in the electronic structure and hot carrier dynamics in anisotropically strain-relaxed RuO_2 (110) films. We note that the critical thickness for anisotropic strain relaxation deduced from the optical spectroscopies is consistent with abrupt changes in the symmetry patterns of the optical SHG above 4 nm of RuO_2/TiO_2 (110) films (*32*). The consistency across independent experiments suggests that strain relaxation begins around 4 nm and dominates the RuO_2 film thickness dependence of various properties. Our epitaxy approach offers a facile method for realizing ultrafast anisotropic electronic dynamics of metallic rutile systems, which is distinct from conventional studies in insulating/semimetal systems (*23*, *25*–*27*). Furthermore, our findings establish a fundamental link between band nesting and transient optical anisotropy, shedding light on the underlying mechanisms governing directional carrier dynamics in metals. This work not only advances the fundamental understanding of strain-driven optical anisotropy in high-symmetry metals but also opens exciting pathways for the design of next-generation optoelectronic devices with precise tunability via epitaxial strain control.

METHODS

Hybrid MBE and structural characterizations

Epitaxial RuO_2 films were grown using an oxide hMBE system (Scienta Omicron) on TiO_2 (110) single-crystalline substrates (Crystec). The substrate treatment process involved cleaning with acetone, methanol, and isopropanol, followed by a 2-hour bake at 200°C in a load lock chamber. Before film growth, a 20-min annealing in oxygen plasma at a growth temperature of 300°C was performed. A metal-organic precursor, $Ru(acac)_3$, was thermally evaporated using a low-temperature effusion cell (MBE Komponenten) with an effusion cell temperature of between 170° and 180°C. The radio frequency oxygen plasma and an oxygen gas pressure of 5×10^{-6} torr were used during the growth. After the growth, the sample was cooled to 120°C in the presence of oxygen plasma to prevent the potential formation of oxygen vacancies. We monitored film surfaces before, during, and after growth using in situ reflection high-energy electron diffraction (Staib Instruments). In addition, we determined the crystallinity, film thickness, roughness, and strain state using XRD (Rigaku SmartLab XE) with reciprocal space mapping, x-ray reflectivity, and θ-2θ measurements. Surface morphologies were measured using atomic force microscopy (Bruker Nanoscope V Multimode 8) with peakforce tapping mode. In this study, we focused on samples with film thicknesses below 20 nm for several reasons: (i) to ensure that the pump-probe experiments remained within the probing depth ~26 nm; (ii) to avoid surface cracking that occurs in films thicker than 20 nm; and (iii) to isolate anisotropic strain relaxation along [001] because we have confirmed that strain relaxation also occurs along the $[1\bar{1}0]$ direction at 26 nm in the previous study (*35*).

Single crystal synthesis

RuO_2 (001) and (110) single crystals were synthesized by sintering a pelletized RuO_2 powder inside an alumina crucible in the air. The pellet was heated up to 1473 K and slowly cooled down to 1023 K at a cooling rate of 1.25 K per hour until the furnace was turned off for quenching. The blue-black metallic crystals were at maximum $1 \times 1 \times 0.5$ mm^3 in size.

DFT calculation

We performed first-principles calculations based on DFT (*51*) as implemented in the Vienna ab initio simulation package (*52*). The projector augmented wave potentials (*53*, *54*) were used to describe the valence electrons, and the plane-wave kinetic energy cutoff was chosen to be 500 eV. The exchange-correlation function was treated by the generalized gradient approximation of Perdew-Burke-Ernzerhof (*55*). The lattice parameters are summarized in table S1. The corresponding Brillouin zones were sampled with a $20 \times 10 \times 10$ *k*-grid mesh. When projecting the density of states, the following notations were used for the coordinate axes: $x = [001]$, $y = [1\bar{1}0]$, and $z = [110]$. The optical conductivity was calculated by the Kubo-Greenwood formula defined as (*56*, *57*)

$$\sigma_{\alpha\beta}(\hbar\omega) = \frac{ie^2\hbar}{N_k\Omega_C}\sum_{\mathbf{k}}\sum_{n,m}\frac{f_{m\mathbf{k}}-f_{n\mathbf{k}}}{\varepsilon_{m\mathbf{k}}-\varepsilon_{n\mathbf{k}}}\frac{\langle\psi_{n\mathbf{k}}|v_\alpha|\psi_{m\mathbf{k}}\rangle\langle\psi_{m\mathbf{k}}|v_\beta|\psi_{n\mathbf{k}}\rangle}{\varepsilon_{m\mathbf{k}}-\varepsilon_{n\mathbf{k}}-(\hbar\omega+i\eta)}$$

where α and β are Cartesian directions, N_k is the total number of *k*-points, and Ω_C is a volume of the unit cell structures. Here, a broadening parameter of η is chosen to be 100 meV. The numerical calculations of $\sigma_{\alpha\beta}(\hbar\omega)$ were performed by the Wannier90 package (*58*). To construct the Wannier Hamiltonian, we used *d* and *p* orbital projections for Ru and O atoms, respectively.

X-ray absorption spectroscopy

O *K*-edge XAS spectra of RuO_2/TiO_2 thin films are measured at the 6A beamline of the Pohang Light Source using TEY measurement, which is sensitive to the film surface. The measurements were conducted at room temperature and surface normal configuration with π (σ) polarization, where the electrical field direction of the x-rays is parallel to the [001] ($[1\bar{1}0]$) crystal direction of RuO_2/TiO_2 (110).

X-ray photoelectron spectroscopy

To confirm the oxidation state of Ru in the RuO_2 films (fig. S5), we performed core-level x-ray photoelectron spectroscopy measurements on the Ru 3*p* region using a Physical Electronics VersaProbe III system equipped with a monochromatic Al Kα x-ray source (1486.6 eV). A flood gun was used to mitigate surface charging effects during photoemission. The spectra were collected with a pass energy of 55 eV and an energy step size of 0.05 eV.

Spectroscopic ellipsometry

To acquire the optical conductivity of RuO_2/TiO_2 (110) heterostructures, we used spectroscopic ellipsometry (M-2000, J. A. Woollam Co. Inc.) with a wavelength range of 0.73 to 6.44 eV and incident angles of 60°, 65°, and 70°. To experimentally access the anisotropic optical response of rutile (110) systems using spectroscopic ellipsometry, we measured each sample twice by rotating the crystal orientation by 90°: (i) *p*-polarization along [001] and *s*-polarization along $[1\bar{1}0]$ and (ii) *p*-polarization along $[1\bar{1}0]$ and *s*-polarization along $[00\bar{1}]$. Details of the anisotropic model are included in text S1. This approach yielded consistent results with previously reported optical constants for bulk TiO_2 (fig. S16). Subsequently, we analyzed the thin-film samples using the same method and meticulously evaluated the dielectric function of the RuO_2 thin film using a uniaxial layer model.

Optical pump-probe experiment

We measured changes in transient reflectivity (ΔR) using the optical pump-probe method to monitor the anisotropic carrier dynamics. The pump and probe beam were separated by a beam splitter from an 80-MHz pulsed laser beam that has 785-nm center wavelength (Vision-S, Coherent). We modulated the pump and probe beam using an electro-optic modulator with 10 MHz and a mechanical chopper with 700 Hz, respectively. Both pump and probe beams were focused on the samples in the normal incidence, using a 5× microscope lens with a beam size of 20 μm. The power of the pump and probe beam was set to be 50 and 3 mW, respectively. To block the pump beam from entering the detector, we used a two-tint method using the sharp-edge long-pass filter and short-pass filter (Semrock). By using a two-channel digital lock-in amplifier (Zürich instrument), we demodulated the signal with side-band frequencies composed of 10 MHz and 700 Hz to achieve the pump-induced reflectivity changes. To focus on the decay of hot carrier dynamics, we extracted the oscillation component from the coherent phonon oscillation in fig. S15.

Electrical transport using Hall bar devices

We fabricated the Hall bar devices along two different in-plane [001] and [110] directions using photolithography followed by argon ion

milling (*49*). We used aluminum (Al) wire bonding for electrical contacts. The electrical conductivities (σ) are measured by using the Quantum Design Dynacool Physical Property Measurement System (PPMS) with a Keithley 2430 source-measure unit.

Supplementary Materials

This PDF file includes:

Supplementary Text S1 and S2
Figs. S1 to S16
Table S1

REFERENCES AND NOTES

1. H. Yuan, X. Liu, F. Afshinmanesh, W. Li, G. Xu, J. Sun, B. Lian, A. G. Curto, G. Ye, Y. Hikita, Z. Shen, S.-C. Zhang, X. Chen, M. Brongersma, H. Y. Hwang, Y. Cui, Polarization-sensitive broadband photodetector using a black phosphorus vertical p–n junction. *Nat. Nanotechnol.* **10**, 707–713 (2015).
2. H.-Y. Hou, S. Tian, H.-R. Ge, J.-D. Chen, Y.-Q. Li, J.-X. Tang, Recent progress of polarization-sensitive perovskite photodetectors. *Adv. Funct. Mater.* **32**, 2209324 (2022).
3. J. Wang, C. Jiang, W. Li, X. Xiao, Anisotropic low-dimensional materials for polarization-sensitive photodetectors: From materials to devices. *Adv. Opt. Mater.* **10**, 2102436 (2022).
4. C. Liu, S. Ding, Q. Tian, X. Hong, W. Su, L. Tang, L. Wang, M. Zhang, X. Liu, Y. Lv, J. C. Ho, L. Liao, X. Zou, Realizing the switching of optoelectronic memory and ultrafast detector in functionalized-black phosphorus/MoS_2 heterojunction. *Laser Photon. Rev.* **17**, 2200486 (2023).
5. X. Wang, A. M. Jones, K. L. Seyler, V. Tran, Y. Jia, H. Zhao, H. Wang, L. Yang, X. Xu, F. Xia, Highly anisotropic and robust excitons in monolayer black phosphorus. *Nat. Nanotechnol.* **10**, 517–521 (2015).
6. Y. Huang, J. Ning, H. Chen, Y. Xu, X. Wang, X. Ge, C. Jiang, X. Zhang, J. Zhang, Y. Peng, Z. Huang, Y. Ning, K. Zhang, Z. Zhang, Mid-infrared black phosphorus surface-emitting laser with an open microcavity. *ACS Photonics* **6**, 1581–1586 (2019).
7. Y. Han, G. Li, Coherent optical communication using polarization multiple-input–multiple-output. *Opt. Express* **13**, 7527–7534 (2005).
8. N. A. Rubin, G. D'Aversa, P. Chevalier, Z. Shi, W. T. Chen, F. Capasso, Matrix Fourier optics enables a compact full-Stokes polarization camera. *Science* **365**, eaax1839 (2019).
9. W. Ran, Z. Ren, P. Wang, Y. Yan, K. Zhao, L. Li, Z. Li, L. Wang, J. Yang, Z. Wei, Z. Lou, G. Shen, Integrated polarization-sensitive amplification system for digital information transmission. *Nat. Commun.* **12**, 6476 (2021).
10. S. H. Suk, S. B. Seo, Y. S. Cho, J. Wang, S. Sim, Ultrafast optical properties and applications of anisotropic 2D materials. *Nanophotonics* **13**, 107–154 (2024).
11. H. Liu, Z. Li, Y. Yu, J. Lin, S. Liu, F. Pang, T. Wang, Nonlinear optical properties of anisotropic two-dimensional layered materials for ultrafast photonics. *Nanophotonics* **9**, 1651–1673 (2020).
12. R. S. Russell, H. P. Nair, K. M. Shen, D. G. Schlom, J. W. Harter, Electronic nematic order in the normal state of strontium ruthenate. *Phys. Rev. B* **108**, L081105 (2023).
13. J. Wu, H. P. Nair, A. T. Bollinger, X. He, I. Robinson, N. J. Schreiber, K. M. Shen, D. G. Schlom, I. Božović, Electronic nematicity in Sr_2RuO_4. *Proc. Natl. Acad. Sci. U.S.A.* **117**, 10654–10659 (2020).
14. J.-H. Chu, J. G. Analytis, K. De Greve, P. L. McMahon, Z. Islam, Y. Yamamoto, I. R. Fisher, In-plane resistivity anisotropy in an underdoped iron arsenide superconductor. *Science* **329**, 824–826 (2010).
15. M.-C. Lee, I. Kwak, Y. Lee, B. Lee, B. C. Park, T. Wolf, T. W. Noh, K. Kim, Nematic response revealed by coherent phonon oscillations in $BaFe_2As_2$. *Phys. Rev. B* **105**, 024501 (2022).
16. S. Liu, C. Zhang, Q. Deng, H.-h. Wen, J.-x. Li, E. E. M. Chia, X. Wang, M. Xiao, Transient electronic anisotropy in overdoped $NaFe_{1-x}Co_xAs$ superconductors. *Phys. Rev. B* **97**, 020505 (2018).
17. C.-W. Luo, P. Chung Cheng, S.-H. Wang, J.-C. Chiang, J.-Y. Lin, K.-H. Wu, J.-Y. Juang, D. A. Chareev, O. S. Volkova, A. N. Vasiliev, Unveiling the hidden nematicity and spin subsystem in FeSe. *NPJ Quantum Mater.* **2**, 32 (2017).
18. C. A. Occhialini, J. J. Sanchez, Q. Song, G. Fabbris, Y. Choi, J.-W. Kim, P. J. Ryan, R. Comin, Spontaneous orbital polarization in the nematic phase of FeSe. *Nat. Mater.* **22**, 985–991 (2023).
19. A. Pal, M. Chinotti, J.-H. Chu, H.-H. Kuo, I. R. Fisher, L. Degiorgi, Optical anisotropy in optimally doped iron-based superconductor. *NPJ Quantum Mater.* **4**, 3 (2019).
20. E. Thewalt, I. M. Hayes, J. P. Hinton, A. Little, S. Patankar, L. Wu, T. Helm, C. V. Stan, N. Tamura, J. G. Analytis, J. Orenstein, Imaging anomalous nematic order and strain in optimally doped $BaFe_2(As,P)_2$. *Phys. Rev. Lett.* **121**, 027001 (2018).
21. M. Yi, D. Lu, J.-H. Chu, J. G. Analytis, A. P. Sorini, A. F. Kemper, B. Moritz, S.-K. Mo, R. G. Moore, M. Hashimoto, W.-S. Lee, Z. Hussain, T. P. Devereaux, I. R. Fisher, Z.-X. Shen, Symmetry-breaking orbital anisotropy observed for detwinned $Ba(Fe_{1-x}Co_x)_2As_2$ above the spin density wave transition. *Proc. Natl. Acad. Sci. U.S.A.* **108**, 6878–6883 (2011).
22. J. He, D. He, Y. Wang, Q. Cui, M. Z. Bellus, H.-Y. Chiu, H. Zhao, Exceptional and anisotropic transport properties of photocarriers in black phosphorus. *ACS Nano* **9**, 6436–6442 (2015).
23. R. J. Suess, M. M. Jadidi, T. E. Murphy, M. Mittendorff, Carrier dynamics and transient photobleaching in thin layers of black phosphorus. *Appl. Phys. Lett.* **107**, 081103 (2015).
24. S. Sim, D. Lee, A. V. Trifonov, T. Kim, S. Cha, J. H. Sung, S. Cho, W. Shim, M.-H. Jo, H. Choi, Ultrafast quantum beats of anisotropic excitons in atomically thin ReS_2. *Nat. Commun.* **9**, 351 (2018).
25. S. B. Seo, S. Nah, M. Sajjad, N. Singh, Y. Shin, Y. Kim, J. Kim, S. Sim, Ultrafast tunable broadband optical anisotropy in two-dimensional ReS_2. *Phys. Rev. Appl.* **18**, 014010 (2022).
26. S. B. Seo, S. Nah, M. Sajjad, J. Song, N. Singh, S. H. Suk, H. Baik, S. Kim, G.-J. Kim, J.-I. Kim, S. Sim, Completely anisotropic ultrafast optical switching and direction-dependent photocarrier diffusion in layered $ZrTe_5$. *Adv. Opt. Mater.* **11**, 2201544 (2023).
27. S. H. Suk, S. Nah, M. Sajjad, S. B. Seo, J. Song, N. Singh, S. Sim, Polarization-driven ultrafast optical switching in TiS_3 nanoribbons via anisotropic hot carrier dynamics. *Adv. Opt. Mater.* **11**, 2300370 (2023).
28. X. Li, H. Liu, C. Ke, W. Tang, M. Liu, F. Huang, Y. Wu, Z. Wu, J. Kang, Review of anisotropic 2D materials: Controlled growth, optical anisotropy modulation, and photonic applications. *Laser Photon. Rev.* **15**, 2100322 (2021).
29. W. Xin, W. Zhong, Y. Shi, Y. Shi, J. Jing, T. Xu, J. Guo, W. Liu, Y. Li, Z. Liang, X. Xin, J. Cheng, W. Hu, H. Xu, Y. Liu, Low-dimensional-materials-based photodetectors for next-generation polarized detection and imaging. *Adv. Mater.* **36**, e2306772 (2024).
30. X. Liu, J. D. Wood, K.-S. Chen, E. Cho, M. C. Hersam, In situ thermal decomposition of exfoliated two-dimensional black phosphorus. *J. Phys. Chem. Lett.* **6**, 773–778 (2015).
31. J. Yuan, Z. Li, W. Yu, Y. Xue, G. Long, Y. Li, H. Mu, D. Li, S. Lin, Structural engineering of two-dimensional black phosphorus towards advanced photonic integrated circuits. *Mater. Des.* **237**, 112547 (2024).
32. S. G. Jeong, I. H. Choi, S. Nair, L. Buiarelli, B. Pourbahari, J. Y. Oh, N. Bassim, A. Seo, W. S. Choi, R. M. Fernandes. Altermagnetic polar metallic phase in ultra-thin epitaxially-strained RuO_2 films. arXiv:2405.05838 [cond-mat.mtrl-sci] (2024).
33. J. P. Ruf, H. Paik, N. J. Schreiber, H. P. Nair, L. Miao, J. K. Kawasaki, J. N. Nelson, B. D. Faeth, Y. Lee, B. H. Goodge, B. Pamuk, C. J. Fennie, L. F. Kourkoutis, D. G. Schlom, K. M. Shen, Strain-stabilized superconductivity. *Nat. Commun.* **12**, 59 (2021).
34. M. Uchida, T. Nomoto, M. Musashi, R. Arita, M. Kawasaki, Superconductivity in uniquely strained RuO_2 films. *Phys. Rev. Lett.* **125**, 147001 (2020).
35. W. Nunn, S. Nair, H. Yun, A. Kamath Manjeshwar, A. Rajapitamahuni, D. Lee, K. A. Mkhoyan, B. Jalan, Solid-source metal–organic molecular beam epitaxy of epitaxial RuO_2. *APL Mater.* **9**, 091112 (2021).
36. R. Berera, R. van Grondelle, J. T. M. Kennis, Ultrafast transient absorption spectroscopy: Principles and application to photosynthetic systems. *Photosynth. Res.* **101**, 105–118 (2009).
37. I. H. Choi, S. G. Jeong, T. Min, J. Lee, W. S. Choi, J. S. Lee, Giant enhancement of electron–phonon coupling in dimensionality-controlled $SrRuO_3$ heterostructures. *Adv. Sci.* **10**, 2300012 (2023).
38. K. H. Bennemann, Ultrafast dynamics in solids. *J. Phys. Condens. Matter* **16**, R995–R1056 (2004).
39. J. B. Goodenough, Metallic oxides. *Progr. Solid State Chem.* **5**, 145–399 (1971).
40. C. A. Occhialini, L. G. P. Martins, S. Fan, V. Bisogni, T. Yasunami, M. Musashi, M. Kawasaki, M. Uchida, R. Comin, J. Pelliciari, Strain-modulated anisotropic electronic structure in superconducting RuO_2 films. *Phys. Rev. Mater.* **6**, 084802 (2022).
41. L. F. Mattheiss, Electronic structure of RuO_2, OsO_2, and IrO_2. *Phys. Rev. B.* **13**, 2433–2450 (1976).
42. M. Abbate, J. B. Goedkoop, F. M. F. de Groot, M. Grioni, J. C. Fuggle, S. Hofmann, H. Petersen, M. Sacchi, Probing depth of soft x-ray absorption spectroscopy measured in total-electron-yield mode. *Surf. Interface Anal.* **18**, 65–69 (1992).
43. C. B. Stagarescu, X. Su, D. E. Eastman, K. N. Altmann, F. J. Himpsel, A. Gupta, Orbital character of O-2*p* unoccupied states near the Fermi level in CrO_2. *Phys. Rev. B* **61**, R9233–R9236 (2000).
44. Y. Ping, G. Galli, W. A. Goddard III, Electronic structure of IrO_2: The role of the metal d orbitals. *J. Phys. Chem. C* **119**, 11570–11577 (2015).
45. H. Jeong, S. G. Jeong, A. Y. Mohamed, M. Lee, W.-s. Noh, Y. Kim, J.-S. Bae, W. S. Choi, D.-Y. Cho, Thickness-dependent orbital hybridization in ultrathin $SrRuO_3$ epitaxial films. *Appl. Phys. Lett.* **115**, 092906 (2019).
46. F. D. Groot, Multiplet effects in X-ray spectroscopy. *Coord. Chem. Rev.* **249**, 31–63 (2005).
47. A. K. Goel, G. Skorinko, F. H. Pollak, Optical properties of single-crystal rutile RuO_2 and IrO_2 in the range 0.5 to 9.5 eV. *Phys. Rev. B* **24**, 7342–7350 (1981).

48. M. Wenzel, E. Uykur, S. Rößler, M. Schmidt, O. Janson, A. Tiwari, M. Dressel, A. A. Tsirlin, Fermi-liquid behavior of nonaltermagnetic RuO_2. *Phys. Rev. B* **111**, L041115 (2025).
49. A. K. Rajapitamahuni, S. Nair, Z. Yang, A. K. Manjeshwar, S. G. Jeong, W. Nunn, B. Jalan, Thickness-dependent insulator-to-metal transition in epitaxial RuO_2 films. *Phys. Rev. Mater.* **8**, 075002 (2024).
50. M. Mittendorff, T. Winzer, E. Malic, A. Knorr, C. Berger, W. A. de Heer, H. Schneider, M. Helm, S. Winnerl, Anisotropy of excitation and relaxation of photogenerated charge carriers in graphene. *Nano Lett.* **14**, 1504–1507 (2014).
51. W. Kohn, L. J. Sham, Self-consistent equations including exchange and correlation effects. *Phys. Rev.* **140**, A1133 (1965).
52. G. Kresse, J. Furthmüller, Efficient iterative schemes for ab initio total-energy calculations using a plane-wave basis set. *Phys. Rev. B* **54**, 11169–11186 (1996).
53. P. E. Blöchl, Projector augmented-wave method. *Phys. Rev. B* **50**, 17953–17979 (1994).
54. G. Kresse, D. Joubert, From ultrasoft pseudopotentials to the projector augmented-wave method. *Phys. Rev. B* **59**, 1758–1775 (1999).
55. J. P. Perdew, K. Burke, M. Ernzerhof, Generalized gradient approximation made simple. *Phys. Rev. Lett.* **77**, 3865–3868 (1996).
56. R. Kubo, Statistical-mechanical theory of irreversible processes. I. General theory and simple applications to magnetic and conduction problems. *J. Phys. Soc. Japan* **12**, 570–586 (1957).
57. D. A. Greenwood, The Boltzmann equation in the theory of electrical conduction in metals. *Proc. Phys. Soc.* **71**, 585–596 (1958).
58. G. Pizzi, V. Vitale, R. Arita, S. Blügel, F. Freimuth, G. Géranton, M. Gibertini, D. Gresch, C. Johnson, T. Koretsune, J. Ibañez-Azpiroz, H. Lee, J.-M. Lihm, D. Marchand, A. Marrazzo, Y. Mokrousov, J. I. Mustafa, Y. Nohara, Y. Nomura, L. Paulatto, S. Poncé, T. Ponweiser, J. Qiao, F. Thöle, S. S. Tsirkin, M. Wierzbowska, N. Marzari, D. Vanderbilt, I. Souza, A. A. Mostofi, J. R. Yates, Wannier90 as a community code: New features and applications. *J. Phys. Condens. Matter* **32**, 165902 (2020).

Acknowledgments

Funding: Film synthesis (S.G.J and B.J.) was supported by the US Department of Energy through grant nos. DE-SC0020211 and (partly) DE-SC0024710. Structural characterization, transport, and ellipsometry (at UMN) were supported by the Air Force Office of Scientific Research (AFOSR) through grant nos. FA9550-21-1-0025 and FA9550-24-1-0169. S.N. was supported partially by the UMN MRSEC program under award no. DMR-2011401. Parts of this work were carried out at the Characterization Facility, University of Minnesota, which receives partial support from the NSF through the MRSEC program under award no. DMR-2011401. The work by J.H.L. and C.K. was supported by the Global Research Development Center (GRDC) Cooperative Hub Program through the National Research Foundation of Korea (NRF) funded by the Ministry of Science and ICT (MSIT) (grant no. RS-2023-00258359) and the NRF grant funded by MSIT (grant no. NRF-2022R1A3B1077234). This work was supported by the National Research Foundation of Korea (NRF) grant funded by the Korean government (MSIT) [nos. RS-2022-NR070254, RS-2024-00486846 (I.H.C. and J.S.L.), 2021R1A2C2011340 (J.Y.O and W.S.C.), RS-2023-00220471 (J.Y.O. and W.S.C.), and RS-2023-00281671 (J.Y.O. and W.S.C.)]. A.S. acknowledges the support of the National Science Foundation grant no. DMR-2104296.
Author contributions: Conceptualization: S.G.J., I.H.C., S.L., J.S.L., T.L., and B.J. Methodology: S.G.J., I.H.C., S.L., J.Y.O., S.N., J.H.L., C.K., A.S., W.S.C., T.L., J.S.L., and B.J. Visualization: S.G.J. and I.H.C. Supervision: J.S.L. and B.J. Writing—original draft: S.G.J., I.H.C., S.L., J.S.L., T.L., and B.J. Writing—review and editing: S.G.J., I.H.C., S.L., J.Y.O., S.N., J.H.L., C.K., A.S., W.S.C., T.L., J.S.L., and B.J. **Competing interests:** The authors declare that they have no competing interests. **Data and materials availability:** All data needed to evaluate the conclusions in the paper are present in the paper and/or the Supplementary Materials.

Submitted 12 February 2025
Accepted 21 May 2025
Published 27 June 2025
10.1126/sciadv.adw7125

ScienceAdvances

Anisotropic strain relaxation-induced directional ultrafast carrier dynamics in RuO_2 films

Seung Gyo Jeong, In Hyeok Choi, Seungjun Lee, Jin Young Oh, Sreejith Nair, Jae Hyuck Lee, Changyoung Kim, Ambrose Seo, Woo Seok Choi, Tony Low, Jong Seok Lee, and Bharat Jalan

Sci. Adv. **11** (26), eadw7125. DOI: 10.1126/sciadv.adw7125

Science Advances (ISSN 2375-2548) is published by the American Association for the Advancement of Science. 1200 New York Avenue NW, Washington, DC 20005. The title *Science Advances* is a registered trademark of AAAS.